Integrated Broadband Mode Division Demultiplexer in Waveguide Arrays

Yu-le Zhao,[*] Chong Sheng, Zi-yi Liu, Shi-ning Zhu, and Hui Liu[†]

National Laboratory of Solid State Microstructures, School of Physics, Collaborative Innovation Center of Advanced Microstructures, Nanjing University, Nanjing 210093, China

On-chip mode division (de)multiplexing plays a significant role in integrated devices to greatly improve communication capacity. One of the goals of mode division (de)multiplexing is to realize devices with larger bandwidth and better fabrication tolerance. However, integrated broadband mode division (de)multiplexing devices have rarely been reported up to now. In this work, we experimentally realize a broadband mode division demultiplexing device with a high degree of fabrication tolerance based on a lithium niobate-on-insulator waveguide array. By taking advantage of the fact that different modes in the waveguide array have different group velocities, we experimentally confirm that different modes in the waveguide array have different transverse displacements. The implementation of the integrated broadband mode division demultiplexer may have future applications in information processing technology, quantum communication, and quantum computing.

DOI: 10.1103/PhysRevApplied.19.064014

I. INTRODUCTION

With the exponential growth of bandwidth demand for on-chip communication and optical fiber communication systems, one of the urgent problems to be solved is expanding the transmission capacity in integrated optical communication systems. To improve the transmission capacity of communication, one can apply wavelength division multiplexing technology [1–3] and space division multiplexing technology [4–6] in communication systems, which provide a high degree of freedom for carrying information. Furthermore, recent years also have witnessed remarkable advances in mode division multiplexing technology, which uses the freedom of the optical orthogonal mode of a single wavelength to increase the optical communication capacity. In particular, this technology can be deployed together with wavelength division multiplexing and polarization multiplexing, so that the communication capacity can be further increased many times. Various types of mode division (de)multiplexing devices have been achieved, including the asymmetric *Y*-junction type [7–9], adiabatic coupling type [10], inverse grating coupling type [11–13], asymmetric directional coupling type [14–18], multimode interference type [19], and inversely designed structures [20,21]. Nevertheless, the design of the asymmetric *Y* junction requires a relatively large footprint, which does not favor integration. The inverse grating coupling type with the subwavelength structure requires a high-precision fabrication technology, but has limited operation bandwidth.

Additionally, the asymmetric directional coupling type not only has a large occupancy area, but also requires the accurate fabrication of the designed structures, and has the disadvantage of narrow working bandwidth. While some research groups have utilized the method of reverse design to realize an ultracompact footprint and improve the working bandwidth, the reverse design method requires a large amount of calculation and accurate sample fabrication technology. Meanwhile, the adiabatic coupler has the advantages of easy design and fabrication among these mode division (de)multiplexing devices, but only supports a few optical modes. To date, most mode division (de)multiplexers are either wavelength sensitive or need high-precision fabrication. Therefore, determining how to realize integrated mode division (de)multiplexing devices with broadband working wavelength and easy fabrication has attracted a large amount of attention.

At the same time, the lithium niobate-on-insulator (LNOI) platform has strong electro-optic, acousto-optic, and thermo-optic effects with a wide transparent window of the wavelength as well as a high refractive index contrast and a nonlinear coefficient, so it has become a promising candidate for integrated photonics. In fact, some basic structures have been developed on the LNOI platform [22–24], such as waveguides [25–27] and microring resonators [28,29]. Moreover, a number of integrated devices have also been developed on this platform, such as the ultracompact on-chip spectrometer [30], electro-optic modulators [31], and optical frequency combs [32]. However, the works about broadband mode division demultiplexing on the LNOI platform have rarely been reported to date.

---

[*]203336849@qq.com
[†]liuhui@nju.edu.cn

In this work, we use multimode waveguide arrays to achieve broadband mode division demultiplexing functionality. This is mainly due to the fact that the group velocity of different modes in this designed structure is mode sensitive but not wavelength sensitive. To realize such devices, we first calculate group velocities of different modes in the lithium niobate thin-film waveguide array using COMSOL Multiphysics (COMSOL Inc.). Then we experimentally fabricate the designed lithium niobate waveguide arrays for the proof of concept of broadband mode division demultiplexers. To experimentally demonstrate mode division demultiplexing in waveguide arrays, several modes are input into the waveguide arrays through the multimode waveguide, and then the transmission paths of different modes are observed through fluorescence imaging. Our results clarify that different modes in the waveguide array have different transverse displacements. Additionally, to exhibit the broadband characteristics of this device, we employ different wavelengths in a certain bandwidth range in this waveguide array. As a result, this broadband mode division demultiplexer can increase the bandwidth density of the on-chip interconnection and

improve the information transmission capacity of the integrated communication system.

II. DEVICE STRUCTURE AND OPERATION PRINCIPLE

To achieve the mode division demultiplexing in waveguide arrays, we first study multiple modes for a single waveguide, and then we study the mode-coupling behavior in two identical waveguides. For a single waveguide as shown in Fig. 1(a), the electromagnetic wave with a wavelength of 445 nm can support multiple modes transmitted within it. Figure 1(a) shows the mode field distribution of several TE modes, including TE_0, TE_1, and TE_2 modes. According to waveguide mode theory, each mode in a multimode waveguide has a different propagation constant and a different mode cross-section area. Furthermore, based on the mode-coupling theory, the same waveguide modes in two adjacent identical multimode waveguides will form symmetric and antisymmetric modes due to coupling, as shown in Figs. 1(b)–1(d). For different waveguide modes, we find that the coupling coefficient increases with the
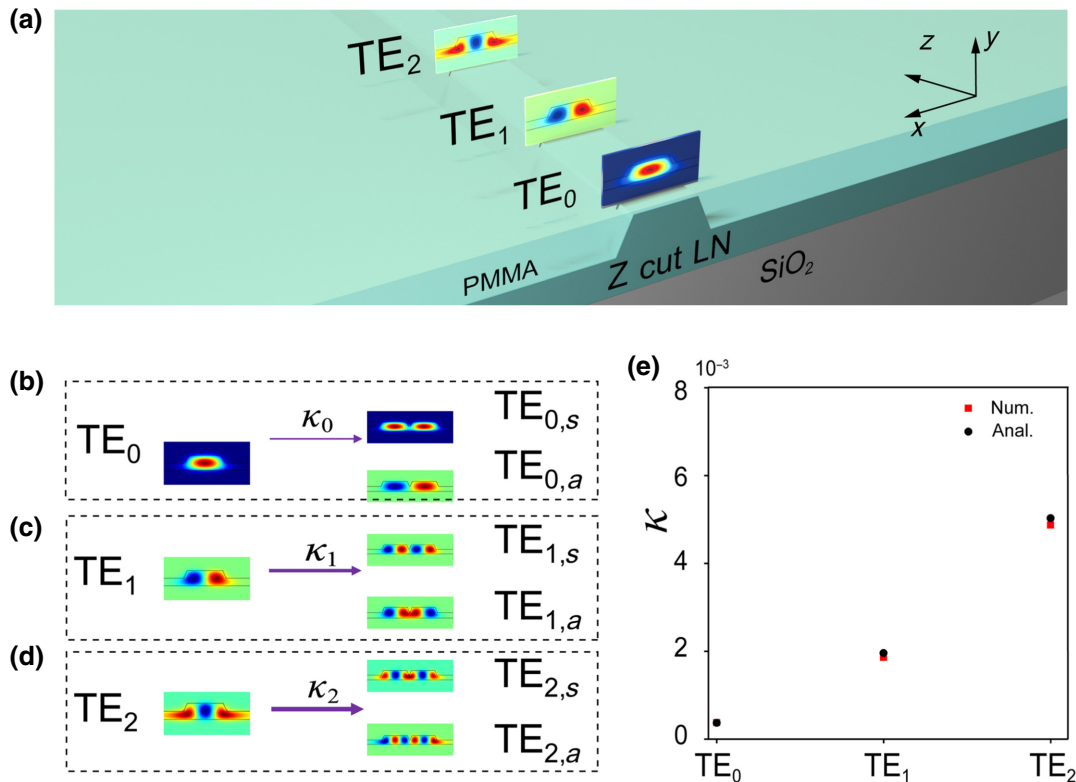

FIG. 1. (a) Schematic of TE modes in an LNOI single multimode waveguide excited by an electromagnetic wave at 445 nm. (b)–(d) Representation of TE_0, TE_1, and TE_2 symmetric and antisymmetric modes with different propagation constants in the coupling of double waveguide systems, in which arrows with different widths represent different coupling coefficients. (e) Comparison of the mode-coupling coefficients obtained by the two methods of calculating coupling coefficients. The results of both calculations are considered similar. The red squares represent the coupling coefficients calculated using the numerical method, and the black circles represent the analytical method.

increasing mode order. Moreover, the propagation constants of symmetric and antisymmetric modes generate disparity owing to the coupling between the waveguides. Remarkably, the relation between the coupling coefficient and the disparity of symmetric and antisymmetric modes can be described as $\kappa_m = (\beta_{m,s} - \beta_{m,a})/2$, where $\beta_{m,s}(\beta_{m,a})$ is the propagation constant of the mth-order symmetric (antisymmetric) mode. The values of $\beta_{m,s}$ and $\beta_{m,a}$ are numerically calculated in COMSOL. We also calculate the coupling coefficients by an analytical method that involves calculating the mode field overlap integral of the waveguide modes [33]. We compare the coupling coefficients calculated by the numerical method with those from the analytical method, and the results calculated by both fit well, as shown in Fig. 1(e).

To study the evolution of different waveguide modes in a waveguide array, we need to analyze the mode dispersion caused by the coupling among the waveguides. According to the coupled-wave theory, the electromagnetic wave transmitted within the waveguide arrays satisfies the following equation [34]:

$$i\frac{da_{n,m}(z)}{dz} + \kappa_m[a_{n-1,m}(z) + a_{n+1,m}(z)] = 0. \quad (1)$$

Here, $a_{n,m}(z)$ represents the amplitude of the mth-order mode electric field in the nth waveguide. The dispersion relation of the mth-order mode in the waveguide arrays can be depicted as $k_{z,m} = \beta_m + 2\kappa_m \cos(k_{x,m}D)$, where β_m is the propagation constant of the mth-order mode in the single waveguide. $k_{x,m}(k_{z,m})$ is the transverse (longitudinal) component of the mth-order mode wave vector. D is the period of the waveguide arrays. According to this formula, the dispersions of the first three TE modes are obtained by an analytical method as shown in Fig. 2(a). In addition to obtaining the periodic dispersion by the analytical method, we also calculate the periodic dispersion by directly simulating the waveguide array in COMSOL. Figure 2(a) shows that the dispersions obtained by the two methods fit well. Then we define the group velocities $V_{x,m}$ and $V_{z,m}$ for the mth-order waveguide mode, which are respectively along the transverse direction and the longitudinal direction. We also define the mode division angle (MDA) of the mth-order mode in the waveguide array as θ_m, which is depicted as $\tan\theta_m = v_{x,m}/v_{z,m} = (d\omega/dk_{x,m})/(d\omega/dk_{z,m}) = dk_{z,m}/dk_{x,m}$, thus $\theta_m = \arctan[dk_{z,m}/dk_{x,m}]$. Details of the numerical method of calculating MDA can be found in Sec. I of the Supplemental Material [35]. During mode transmission from a single waveguide to a waveguide array, the propagation constants of the mth-order mode need to satisfy the conservation condition, which can be depicted as $k_{z,m} = \beta_m$, where β_m is the propagation constant of the mth-order mode in the single waveguide. Considering also $k_{z,m} = \beta_m + 2\kappa_m \cos(k_{x,m}D)$,
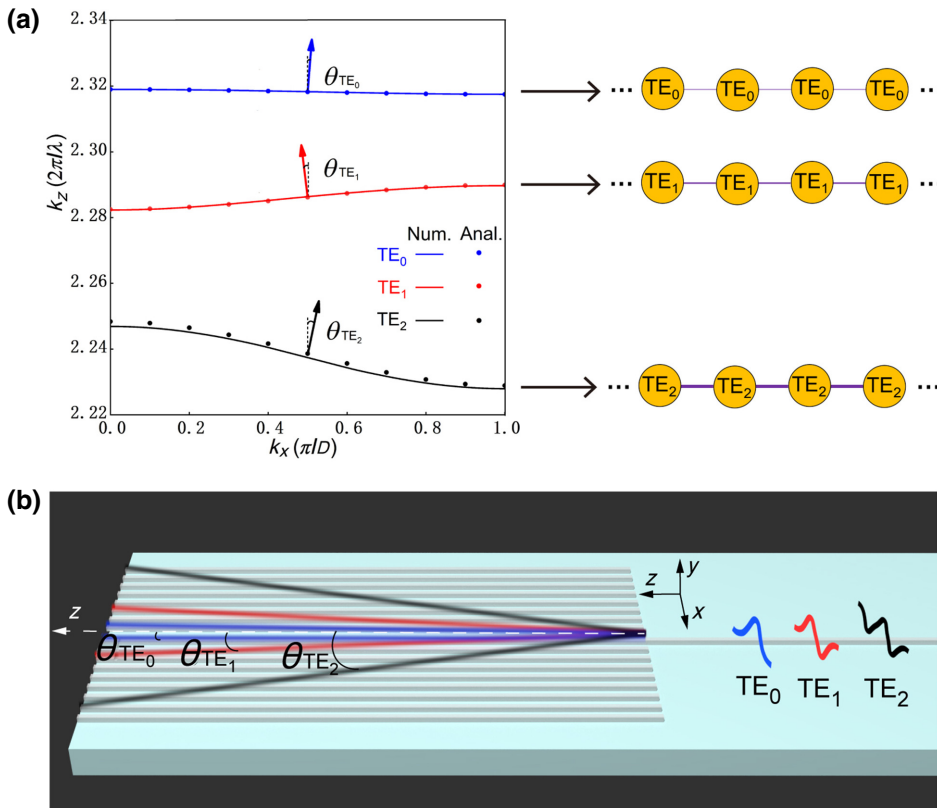

FIG. 2. (a) Comparison of the periodic dispersions of three modes obtained from the numerical method and the analytical method. The numerical method is represented by the solid line shown in the figure. The analytical method of calculating the dispersion is shown as dotted lines in the figure where the arrow represents the group velocity dispersion direction (MDA) of each TE mode, and each dispersion corresponds to a one-dimensional atomic chain model. (b) Schematic diagram of transmission of TE_0, TE_1, and TE_2 modes in waveguide array.

we then know that $k_{x,m} = \pi/2D$. Finally, we can obtain the following formula:

$$\theta_m = \arctan(-2D\kappa_m). \quad (2)$$

This formula gives the calculation for the MDA. From the formula, we can find that the larger the coupling coefficient (larger mode order), the larger the MDA in the waveguide array will be, as shown in Fig. 2(b).

When considering the different wavelengths of the incident electromagnetic wave, we can also calculate the dispersion curve corresponding to the specific mode of each wavelength, as can be seen in Fig. 3(a), which shows $kz(kx, \lambda)$ for several modes for wavelengths from 405 to 505 nm. In the surface diagram, the three surfaces from top to bottom represent TE_0, TE_1, and TE_2 in turn. The arrows of different colors on the dispersion curves indicate the different modes of the MDA. To explore the broadband potential of the scheme, we need to analyze the variation of the MDA with wavelength as illustrated in Fig. 3(a). Therefore, we calculate the curve of the MDA with wavelength, as shown in Fig. 3(b). The values denoted by the inverted triangles in Fig. 3(b) are directly obtained from the experimental data, indicating the MDA of the three TE modes when several wavelengths selected in the experimental test are excited. We find that the MDA of each mode increases with the increase of wavelength between 405 and 505 nm, and the MDA of the lower-order mode increases more slowly than that of the higher-order mode. When the excitation wavelength of the TE_2 mode is changed from 405 to 505 nm, the MDA changes by about 4°. Consequently, the MDA increases slowly with the wavelength. It can be inferred that the designed waveguide array structure can achieve mode division demultiplexing

in a relatively wide wavelength range, and can be used as a broadband mode demultiplexing device.

III. SAMPLE FABRICATION AND EXPERIMENTAL TESTING

The design principles described previously for broadband mode division demultiplexing are applicable to many material platforms, including silicon-on-insulator and silicon nitride, etc. In each material platform corresponding to the waveguide array system, the MDA of the corresponding mode can be calculated based on group velocity theory. In this experiment, we fabricate the broadband mode division demultiplexer based on LNOI. First, we drill the waveguide arrays with a focused ion beam, together with the couple-in tapers and gratings. The SEM of the lithium niobate waveguide arrays is shown in Figs. 4(a) and 4(b), where the detailed structural parameters can be found in Sec. III of the Supplemental Material [36]. The grating coupler can couple the laser into a single multimode waveguide, where the excited TE_0, TE_1, and TE_2 modes are introduced into the waveguide arrays by the single multimode waveguide. In the second step, to directly observe the mode transmission path, we use rare-earth fluorescence imaging technology. The europium-doped PMMA solution emits fluorescence in the 610-nm band when it is irradiated by a 400–500-nm waveguide laser. The fluorescent material used here is a common commercial fluorescent material with a luminous wavelength of 610 nm that can be excited by shorter wavelengths. Indeed, if we can find a fluorescent material with a luminescence wavelength larger than 2 μm, then we may utilize the communication band (near 1550 nm) for experimental testing. We prepare a PMMA solution containing europium by mixing
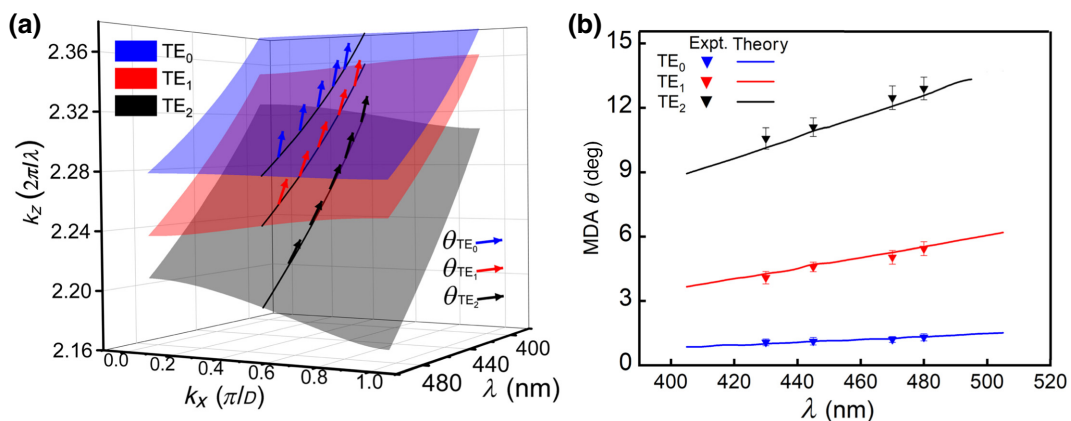

FIG. 3. (a) In the wavelength range of 405 to 505 nm, the dispersion surface is formed by the coupling of the same TE mode in the waveguide array, and the arrow on the dispersion curve indicates the MDA of the corresponding mode in the waveguide array. (b) The solid line in the figure is the MDA of several TE modes in the wavelength range of 405 to 505 nm calculated by COMSOL. The values for the inverted triangles are obtained directly from the experimental data, indicating the MDA of the three TE modes when several wavelengths selected in the experimental test are excited. The $\pm$ standard deviation range of the measured data is displayed by the error bar.
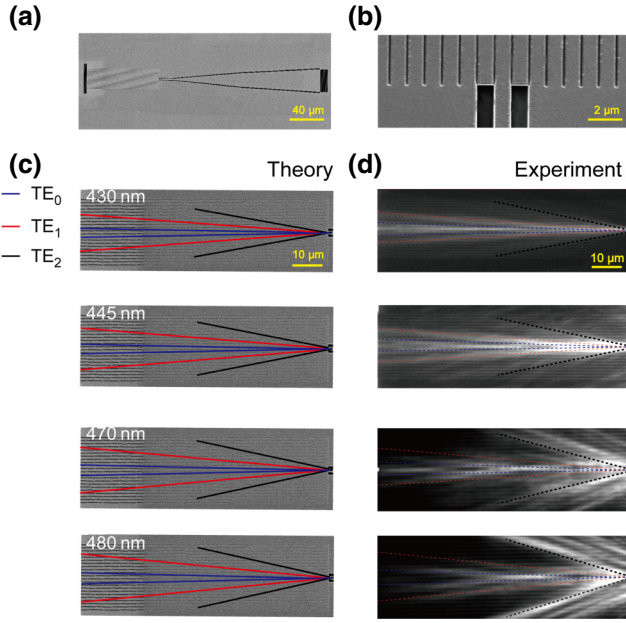
FIG. 4.   (a) SEM image of lithium niobate waveguide array sample. (b) An enlarged SEM image of the connection between a single multimode waveguide and the waveguide array of sample. (c) The propagation diagram of several TE modes at 430-, 445-, 470-, and 480-nm excitation calculated by group velocity theory. (d) The transmission diagrams of several TE modes at 430-, 445-, 470-, and 480-nm excitation measured experimentally.

PMMA particles with rare-earth europium particles in a toluene solution. The detailed preparation process of the PMMA solution can be found in Sec. III of the Supplemental Material [37]. After preparing the waveguide arrays and europium-doped PMMA solution, we spin the solution onto the lithium niobate chip through a homogenizer and obtain a sample of the waveguide arrays that suit our experimental observation requirements [38]. Here, we choose the appropriate PMMA concentration and spin-coating thickness so that we obtain a good fluorescence effect.

To demonstrate broadband mode division demultiplexing, we utilize the prepared samples for experimental testing. In the experimental demonstration, we couple 430-, 445-, 470-, and 480-nm lasers into the waveguide arrays through the grating coupler. Different modes are transmitted in the waveguide array, and the mode transmission paths are revealed by fluorescence imaging. Because we need to observe the 610-nm fluorescence image, we use a filter for filtering the short-wavelength laser and a scientific CMOS (sCMOS) camera (Hamamatsu, ORCA-Flash 4.0, C11440-42U) to capture images of the mode transmission path. The images of the mode transmission paths at different wavelengths are shown in Fig. 4(d), in which mode transmission paths at different angles represent different modes of transmission. Correspondingly, Fig. 4(c) shows the transmission schematic corresponding to TE modes excited at different wavelengths calculated by group velocity theory. It can be seen that the experimental results and theoretical prediction results under several wavelengths of excitation within a certain bandwidth are in good agreement. We extract the average value of the mode angle obtained from the experimental test and compare it with the mode angle obtained from the theoretical calculation, as shown in Table I. There is a slight deviation between the experimental test angle and the theoretical prediction angle, but the deviation is within a reasonable range. This discrepancy may arise from deviations in sample preparation. In addition, comparing the fluorescence trajectories excited at different wavelengths in Fig. 4(d), we can find that the mode energy percentage is different. On the one hand, this may be due to the different coupling efficiencies of the gratings at different wavelengths; on the other hand, it may be caused by the tolerance of sample processing. Detailed experimental tests can be obtained in Sec. III of the Supplemental Material [39]. Given the above, this experiment realizes the conceptual verification of broadband mode division demultiplexing based on LNOI.

IV. DISCUSSION

In addition to focusing on the broadband characteristics of mode division demultiplexing, we are also interested in the fabrication tolerance properties of waveguide array mode division demultiplexing devices. Therefore, we also theoretically calculate the influence of different sidewall inclination angles on the MDA. The results are shown in Fig. S1(b) in the Supplemental Material [40]. It is found that the sidewall inclination angle has little effect on the MDA. That is, the different sidewall inclination angles caused by fabricating factors have little effect on the MDA.

TABLE I.   The table shows the theoretically calculated MDA and experimentally tested MDA when the wavelength of the laser is 430, 445, 470, and 480 nm, respectively.

	430 nm		445 nm		470 nm		480 nm	
	Theory (deg)	Expt. (deg)	Theory (deg)	Expt. (deg)	Theory (deg)	Expt. (deg)	Theory (deg)	Expt. (deg)
θ_{TE0}	1.01	1.08	1.13	1.12	1.24	1.21	1.33	1.31
θ_{TE1}	4.27	4.08	4.71	4.55	5.26	5.03	5.52	5.44
θ_{TE2}	10.15	10.56	11.01	11.21	12.07	12.97	12.57	13.72

As a result, the mode division demultiplexing realized by the lithium niobate waveguide arrays has good fabrication tolerance. To improve the efficiency and performance of the mode division demultiplexer, we further optimize the design by propagation simulation. In the propagation simulation, we define the mode energy output port of the demultiplexer, while we calculate the mode demultiplexing efficiency. The results show that the mode demultiplexing efficiency is wavelength insensitive, which indicates that the device has the potential for broadband operation. Detailed propagation simulation results and analysis can be found in Appendices A–C. Fluorescence characterization allows us to directly see the transmission path of the light field, which makes it convenient for us to visually judge the transmission path of the mode. Moreover, another measurement technique has attracted our attention, i.e., imaging the output facet of the waveguide array. This measurement technique offers cleaner data with more information. We will try to use this measurement method in our future experiments. The design principle of the mode division demultiplexer we use can theoretically support more modes. In addition, using the same operating principle, we can tune the device parameters to support higher-order modes for mode division demultiplexing.

V. SUMMARY AND OUTLOOK

In this work, we experimentally achieve mode division demultiplexing by exploiting the group velocity difference of different modes in an LNOI waveguide array. We begin by theoretically analyzing waveguide array mode division demultiplexing and then conceptually verify the broadband property of waveguide array mode division demultiplexing through experiments. Specifically, different modes have different transmission angles for the input direction of a single waveguide, which causes the output modes to be located at different output ports, thus realizing the path allocation of different modes. By adjusting the structure of a uniform waveguide array, such as the gap between waveguides and the width of waveguides, we can design a mode demultiplexer that meets our requirements. Moreover, the mode transmission angle is mode sensitive but not wavelength sensitive. Therefore, a uniform waveguide array with a certain structure has the function of a broadband mode division demultiplexer. On the one hand, LNOI has a high nonlinear coefficient and is a good candidate for preparing efficient quantum entangled light sources. On the other hand, encoding quantum signals in a waveguide mode is conducive to improving the speed of quantum information processing. Therefore, the integrated broadband mode division demultiplexing realized on LNOI may pave the way for quantum photonic integrated circuit–based quantum information processing. Further, the nonuniform waveguide array has more adjustable parameters, such as waveguide width, the gap between waveguides, etc. Thus, the nonuniform waveguide array mode division demultiplexer could improve the device performance compared with the uniform waveguide array mode division demultiplexer. Typically, the high second-order nonlinear coefficients of lithium niobate is conducive for the application of a frequency down-conversion device. Therefore, with an appropriate waveguide array structure design, we can achieve mode division demultiplexing during frequency down-conversion, which could further increase the transmission capacity in integrated optical communication systems. At the same time, lithium niobate possesses a strong electro-optical effect and is a popular material platform for electro-optical modulators. Therefore, the integration of electro-optical modulators and mode division demultiplexers may lead to interesting physics, such as the implementation of switch modes post sorting, which is what we want to explore in the future.
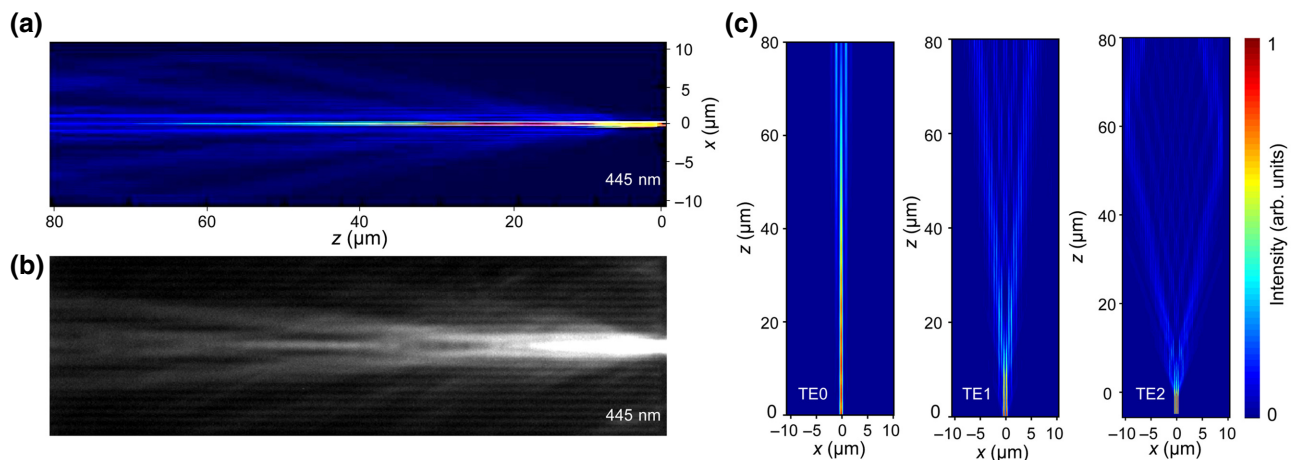

FIG. 5. (a) The schematic of mode division demultiplexing for TE_0, TE_1, and TE_2 mode energy ratios of 50%, 25%, and 25%, respectively. (b) Fluorescence trajectory of the mode under 445-nm excitation. (c) The simulation result presents an aerial view of the 80-μm light field transmission for the three modes.

APPENDIX A: THE SIMULATION OF MODE TRANSMISSION AND ITS COMPARISON WITH EXPERIMENTAL RESULTS

In this work, we utilize grating couplers to excite multiple modes. While we acknowledge that the excitation method may not be as precise as desired, and the energy ratio for different modes cannot be strictly controlled, our main objective is to demonstrate a unique approach for broad mode division demultiplexing with high efficiency. We note that precise control of mode division multiplexing is currently a hot topic of research, and various techniques have been employed in pursuit of this goal for more precise control of information transmission. In future work, we will explore the use of broadband couplers to couple modes of different orders into the waveguide array in hopes of improving control over the process.

Although we cannot yet control the energy ratio for different waveguide modes with a high degree of accuracy, we can confirm that different waveguide modes have been generated using grating coupling. This point is well demonstrated through the three-dimensional finite-difference time domain (FDTD) simulation, as shown in Fig. 5(c), which depicts the propagation simulation of different waveguide modes under 445-nm excitation. To compare with the experimental results, we assume that the energy ratios of TE_0, TE_1, and TE_2 modes are 50%, 25%, and 25%, respectively. Using data matrix processing software, we obtain the propagation light field diagram shown in Fig. 5(a), which closely resembles the experimental result shown in Fig. 5(b). This agreement between our experimental and simulation results strengthens our confidence in our observations and conclusions.

APPENDIX B: OPTIMIZING THE MODE INPUT METHOD

It has come to our attention that existing mode demultiplexers incur an efficiency loss of 3 dB. To address this issue, we explore the boundary waveguide excitation method. Specifically, we conduct propagation simulations using FDTD simulations, as depicted in Figs. 6(a) and 6(c). When exciting the TE_2 mode from the waveguide at the boundary, we observe that it is transmitted to the right side of the waveguide array, as shown in Fig. 6(c). This result contrasts with those obtained using middle waveguide excitation, as presented in Fig. 6(a). Additionally, Figs. 6(b) and 6(d) illustrate the mode distributions at the
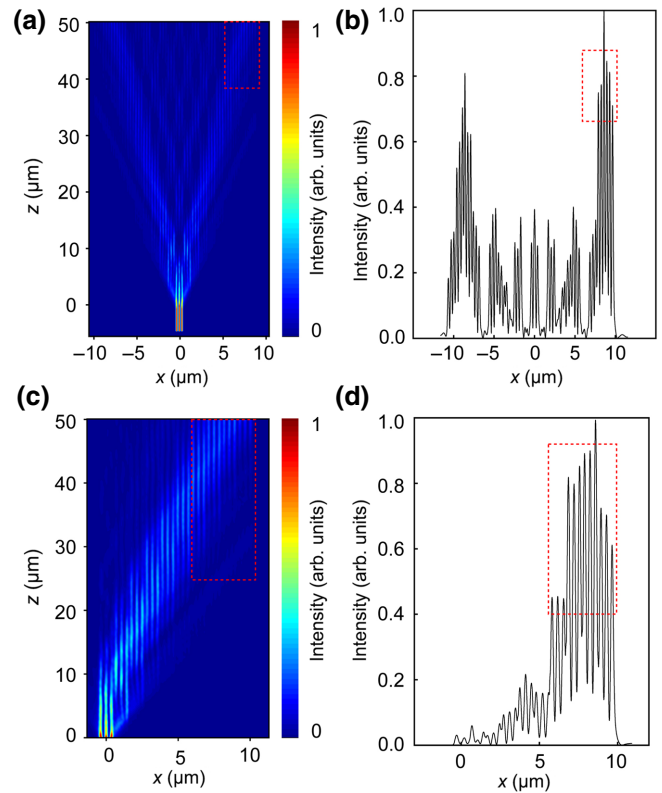

FIG. 6. (a) Top view of transmission power when the TE_2 mode at 445 nm is input from the middle waveguide. (b) Power distribution at the output facet of the waveguide array in (a). The red dotted line box in the figure represents the area selected for multiplexing efficiency calculation. Each red dotted line box contains four waveguides. The mode demultiplexing efficiency is defined as the ratio of the output power in the red dashed box region to the input power. The demultiplexing efficiency shown in (b) is 29%. (c) Top view of transmission power when the TE_2 mode at 445 nm is input from the boundary waveguide. (d) Power distribution at the output facet of the waveguide array in (c). The corresponding multiplexing efficiency in (d) is 88.3%.

output facet for boundary and middle waveguide excitation, respectively. Furthermore, we calculate the mode demultiplexing efficiency for both excitation methods. We define this efficiency as the ratio of output power in the defined output port [indicated by the red dashed box region in Figs. 6(b) and 6(d)] to the input power of the main input waveguide. Our results demonstrate that the mode demultiplexing efficiencies for boundary and middle waveguide excitation are 29.1% and 88.3%, respectively.

APPENDIX C: THE DESIGN OF OUTPUT PORTS AND THE CALCULATION OF DEMULTIPLEXING EFFICIENCY

To further investigate the broadband properties of our device, we design an output port in our propagation simulation, as illustrated in Fig. 7(a). This port is defined as
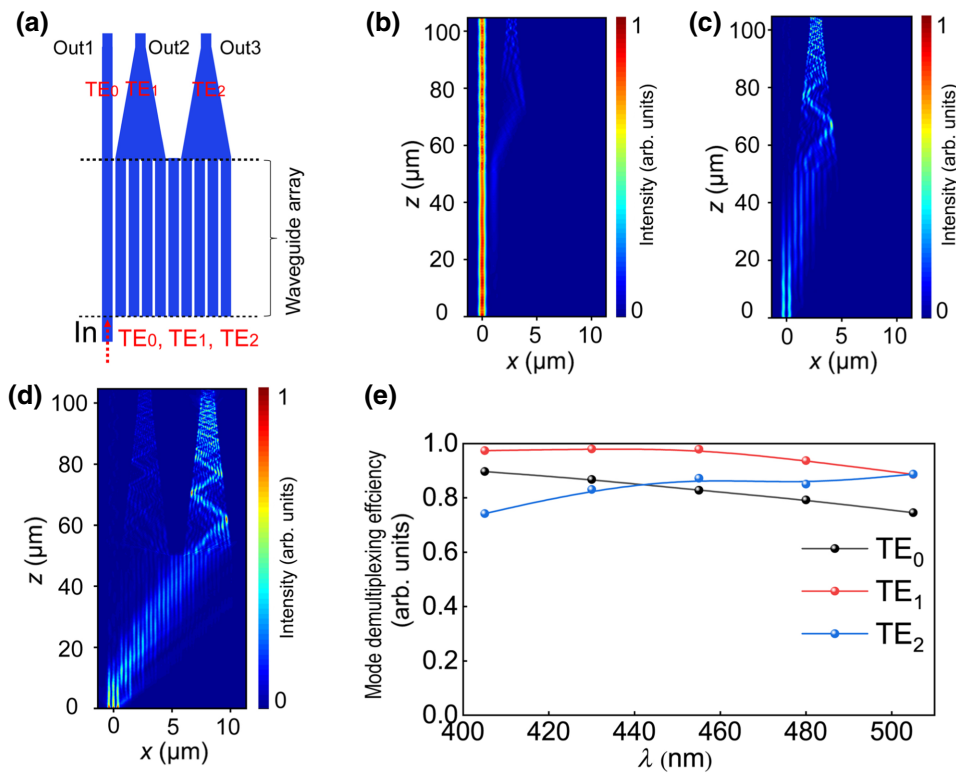
FIG. 7. (a) Schematic diagram of a mode division demultiplexer with output ports. (b) Top view of the transmission path of TE_0 mode in the demultiplexer when simulating 405-nm excitation. (c) Top view of the transmission path of TE_1 mode in the demultiplexer when simulating 405-nm excitation. (d) Top view of the TE_2 mode transmission path in the demultiplexer when simulating 405-nm excitation. (e) Schematic of demultiplexing efficiency of TE_0, TE_1, and TE_2 modes in the wavelength range of 405 to 505 nm.

the mode energy output port (MEOP) and comprises a waveguide directly connected to the main input waveguide, labeled Out0, for the TE_0 mode. The MEOP for the TE_1 mode is a tapered waveguide connecting with the second to fifth waveguides, labeled Out1, while for the TE_2 mode, it is a tapered waveguide connecting with the sixth to tenth waveguides, labeled Out2. As demonstrated in Figs. 7(b)–7(d), when using a 405-nm excitation wavelength, the power distribution of the TE_0 mode is mainly concentrated on the main waveguide. Conversely, the power distributions of the TE_1 and TE_2 modes are concentrated on the second to fifth and sixth to tenth waveguides, respectively. This arrangement enables us to route the energy of each mode to the corresponding MEOP.

We calculate the mode demultiplexing efficiency for each mode at a certain bandwidth using the ratio of output power in the defined output port to the input power of the main input waveguide. As indicated in Fig. 7(e), when the excitation wavelength is varied from 405 to 505 nm, the mode demultiplexing efficiencies of the TE_0, TE_1, and TE_2 modes vary slowly with wavelength. These results suggest that our designed mode division demultiplexer exhibits relatively high demultiplexing efficiency for each mode at a bandwidth of 100 nm. Although we have not yet carried out relevant experiments, our simulations indicate that our devices possess broadband operation capabilities. Therefore, we plan to experimentally route several different transverse waveguide modes to the different output ports of the waveguide array in future work.

[1] F. Hu, H. Yi, and Z. Zhou, Wavelength demultiplexing structure based on arrayed plasmonic slot cavities, Opt. Lett. **36**, 1500 (2011).

[2] G. Wang, H. Lu, and X. Liu, Tunable multi-channel wavelength demultiplexer based on MIM plasmonic nanodisk resonators at telecommunication regime, Opt. Express **19**, 3513 (2011).

[3] E. Laux, C. Genet, T. Skauli, and T. W. Ebbesen, Plasmonic photon sorters for spectral and polarimetric imaging, Nat. Photonics **2**, 161 (2008).

[4] B. y. Zhu, T. F. Taunay, M. F. Yan, M. Fishteyn, G. Oulundsen, and D. Vaidya, 70-Gb/s multicore multimode fiber transmissions for optical data links, IEEE Photonics Technol. Lett. **22**, 1647 (2010).

[5] L. Yuan, Z. Liu, and J. Yang, Coupling characteristics between single-core fiber and multicore fiber, Opt. Lett. **31**, 3237 (2006).

[6] J. M. FINI, B. Y. ZHU, and T. F. Taunay, Statistics of crosstalk in bent multicore fibers, Opt. Express **18**, 15122 (2010).

[7] J. D. Love and N. Riesen, Single-, few-, and multimode Y-junctions, J. Lightwave Technol. **30**, 304 (2012).

[8] N. Riesen and J. D. Love, Design of mode-sorting asymmetric Y-junctions, Appl. Opt. **51**, 2778 (2012).

[9] Z. Zhang, Y. Yu, and S. Fu, Broadband on-chip mode-division multiplexer based on adiabatic couplers and symmetric Y-junction, IEEE Photonics J. **9**, 6600406 (2017).

[10] J. Xing, Z. Li, X. Xiao, J. Yu, and Y. Yu, Two-mode multiplexer and demultiplexer based on adiabatic couplers, Opt. Lett. **38**, 3468 (2013).

[11] Y. He, Y. Zhang, H. Wang, L. Sun, and Y. Su, Design and experimental demonstration of a silicon multi-dimensional (de)multiplexer for wavelength-, mode- and polarization-division (de)multiplexing, Opt. Lett. **45,** 2846 (2020).

[12] H. Qiu, H. Yu, T. Hu, G. Jiang, H. Shao, P. Yu, J. Yang, and X. Jiang, Silicon mode multi/demultiplexer based on multimode grating-assisted couplers, Opt. Express **21,** 17904 (2013).

[13] C. Gui, Y. Gao, Z. Zhang, and J. Wang, On-chip silicon two-mode (de)multiplexer for OFDM/OQAM data transmission based on grating-assisted coupler, IEEE Photonics J. **7,** 7905807 (2015).

[14] L. W. Luo, N. Ophir, C. P. Chen, L. H. Gabrielli, C. B. Poitras, K. Bergmen, and M. Lipson, WDM-compatible mode-division multiplexing on a silicon chip, Nat. Commun. **5,** 3069 (2014).

[15] J. Wang, S. He, and D. Dai, On-chip silicon 8-channel hybrid (de)multiplexer enabling simultaneous mode- and polarization-division-multiplexing, Laser Photonics Rev. **8,** L18 (2014).

[16] L. T. Feng, M. Zhang, Z.-Y. Zhou, M. Li, X. Xiong, L. Y., B.-S. Shi, G.-P. Guo, D.-X. Dai, X.-F. Ren, and G.-C. Guo, On-chip coherent conversion of photonic quantum entanglement between different degrees of freedom, Nat. Commun. **7,** 11985 (2016).

[17] X. Han, X. Han, Y. Jiang, A. Frigg, H. Xiao, P. Zhang, T. G. Nguyen, A. Boes, J. Yang, G. Ren, Y. Su, A. Mitchell, and Y. Tian, Mode and polarization-division multiplexing based on silicon nitride loaded lithium niobate on insulator platform, Laser Photonics Rev. **16,** 2100529 (2021).

[18] X. Wang, H. Yu, Q. Zhang, Z. Fu, P. Xia, Q. Huang, N. Ning, Z. Wei, Y. Wang, X. Jiang, and J. Yang, Ultra-compact silicon mode (de)multiplexer based on directional couplers with subwavelength sidewall corrugations, Opt. Lett. **47,** 2198 (2022).

[19] T. Uematsu, Y. Ishizaka, Y. Kawaguchi, K. Saitoh, and M. Koshiba, Design of a compact two-mode multi/demultiplexer consisting of multimode interference waveguides and a wavelength-insensitive phase shifter for mode-division multiplexing transmission, J. Lightwave Technol. **30,** 2421 (2012).

[20] W. Chang, L. Lu, X. Ren, D. Li, Z. Pan, M. Cheng, D. Liu, and M. Zhang, Ultra-compact mode (de) multiplexer based on subwavelength asymmetric Y-junction, Opt. Express **26,** 8162 (2018).

[21] H. Xie, Y. Liu, S. Wang, Y. Wang, Y. Yao, Q. Song, J. Du, Z. He, and K. Xu, Highly compact and efficient four-mode multiplexer based on pixelated waveguides, IEEE Photonics Technol. Lett. **32,** 166 (2020).

[22] J. Ma, J. Chen, M. Ren, W. Wu, W. Cai, and J. Xu, Second-harmonic generation and its nonlinear depolarization from lithium niobate thin films, Opt. Lett. **45,** 145 (2019).

[23] Y. Qi and Y. Li, Integrated lithium niobate photonics, Nanophotonics **9,** 1287 (2020).

[24] S. Jin, L. Xu, H. Zhang, and Y. Li, LiNbO$_3$ thin-film modulators using silicon nitride surface ridge waveguides, IEEE Photonics Technol. Lett. **28,** 736 (2016).

[25] M. Zhang, W. Ai, K. Chen, W. Jin, and K. S. Chiang, A lithium-niobate waveguide directional coupler for switchable mode multiplexing, IEEE Photonics Technol. Lett. **30,** 1764 (2018).

[26] L. Cai, R. Kong, Y. Wang, and H. Hu, Channel waveguides and y-junctions in x-cut single-crystal lithium niobate thin film, Opt. Express **23,** 29211 (2015).

[27] L. Chang, M. H. P. Pfeiffer, N. Volet, M. Zervas, J. D. Peters, C. L. Manganelli, E. J. Stanton, Y. Li, T. J. Kippenberg, and J. E. Bowers, Heterogeneous integration of lithium niobate and silicon nitride waveguides for wafer-scale photonic integrated circuits on silicon, Opt. Lett. **42,** 803 (2017).

[28] M. Zhang, B. Buscaino, C. Wang, A. Shams-Ansari, C. Reimer, R. Zhu, J. M. Kahn, and M. Loncar, Broadband electro-optic frequency comb generation in a lithium niobate microring resonator, Nature **568,** 373 (2019).

[29] L. Chen and R. M. Reano, Compact electric field sensors based on indirect bonding of lithium niobate to silicon microrings, Opt. Express **20,** 4032 (2012).

[30] D. Pohl, M. R. Escalé, M. Madi, F. Kaufmann, P. Brotzer, A. Sergeyev, B. Guldimann, P. Giaccari, E. Alberti, U. Meier, and R. Grange, An integrated broadband spectrometer on thin-film lithium niobate, Nat. Photonics **14,** 24 (2019).

[31] C. Wang, M. Zhang, X. Chen, M. Bertrand, A. Shams-Ansari, S. Chandrasekhar, P. Winzer, and M. Lončar, Integrated lithium niobate electro-optic modulators operating at CMOS-compatible voltages, Nature **562,** 101 (2018).

[32] Y. He, Q.-F. Yang, J. Ling, R. Luo, H. Liang, M. Li, B. Shen, H. Wang, K. Vahala, and Q. Lin, Self-starting bi-chromatic LiNbO$_3$ soliton microcomb, Optica **6,** 1138 (2019).

[33] K. Okamoto, *Fundamentals of Optical Waveguides*, 2nd ed. (Academic Press, Burlington, MA, USA, 2006).

[34] T. Pertsch, T. Zentgraf, U. Peschel, A. Brauer, and F. Lederer, Anomalous Refraction and Diffraction in Discrete Optical Systems, Phys. Rev. Lett. **88,** 093901 (2002).

[35] See the Supplemental Material at http://link.aps.org/supplemental/10.1103/PhysRevApplied.19.064014 for a method for calculating MDA in periodic dispersion.

[36] See the Supplemental Material at http://link.aps.org/supplemental/10.1103/PhysRevApplied.19.064014 for fabrication of waveguide arrays.

[37] See the Supplemental Material at http://link.aps.org/supplemental/10.1103/PhysRevApplied.19.064014 for preparation of europium doped PMMA solution.

[38] See the Supplemental Material at http://link.aps.org/supplemental/10.1103/PhysRevApplied.19.064014 for PMMA solution spin coating.

[39] See the Supplemental Material at http://link.aps.org/supplemental/10.1103/PhysRevApplied.19.064014 for experimental measurement.

[40] See the Supplemental Material at http://link.aps.org/supplemental/10.1103/PhysRevApplied.19.064014 for relationship between MDA and waveguide sidewall inclination angle.